JGR Solid Earth

Key Points:

- We present a 2-D shear velocity model of the top 16 km of the crust in south-central Alaska across the Alaska range
- The Denali fault was identified as a narrow localized low-velocity anomaly extending to at least 12 km depth
- We observe a low-velocity zone ~12 km beneath the volcanic gap. We interpret the anomaly as a subduction-related magma reservoir

Correspondence to:

S. Rabade,
san.rabade@utah.edu

The Crustal Magmatic Structure Beneath the Denali Volcanic Gap Imaged by a Dense Linear Seismic Array

Santiago Rabade[1] , **Fan-Chi Lin[1]** , **Carl Tape[2]** , **Kevin M. Ward[3]** , **Trevor Waldien[3]** , **and Amir Allam[1]**

[1]Department of Geology and Geophysics, University of Utah, Salt Lake City, UT, USA, [2]Geophysical Institute and Department of Geosciences, University of Alaska, Fairbanks, AK, USA, [3]Department of Geology and Geological Engineering, South Dakota School of Mines & Technology, Rapid City, SD, USA

Abstract The crustal structure in south-central Alaska has been influenced by terrane accretion, flat slab subduction, and a modern strike-slip fault system. Within the active subduction system, the presence of the Denali Volcanic Gap (DVG), a ~400 km region separating the active volcanism of the Aleutian Arc to the west and the Wrangell volcanoes to the east, remains enigmatic. To better understand the regional tectonics and the nature of the volcanic gap, we deployed a month-long north-south linear geophone array of 306 stations with an interstation distance of 1 km across the Alaska Range. By calculating multi-component noise cross-correlation and jointly inverting Rayleigh wave phase velocity and ellipticity across the array, we construct a 2-D shear wave velocity model along the transect down to ~16 km depth. In the shallow crust, we observe low-velocity structures associated with sedimentary basins and image the Denali fault as a narrow localized low-velocity anomaly extending to at least 12 km depth. About 12 km, below the fold and thrust fault system in the northern flank of the Alaska Range, we observe a prominent low-velocity zone with more than 15% velocity reduction. Our velocity model is consistent with known geological features and reveals a previously unknown low-velocity zone that we interpret as a magmatic feature. Based on this feature's spatial relationship to the Buzzard Creek and Jumbo Dome volcanoes and the location above the subducting Pacific Plate, we interpret the low-velocity zone as a previously unknown subduction-related crustal magma reservoir located beneath the DVG.

Plain Language Summary The Alaska Range in south-central Alaska has been shaped by different geological processes. One puzzling aspect is the Denali Volcanic Gap, a region of about 400 km between the Aleutian Arc and the Wrangell volcanoes. To understand this volcanic gap and regional tectonics better, we obtained a 2-D model of shear wave velocity down to a depth of about 16 km, using a month-long linear geophone array with over 300 stations placed at 1 km intervals across the Alaska Range. In the shallow crust, we found areas with low-velocity associated with sedimentary basins. We observe a narrow anomaly related to the Denali fault with low-velocity extending to at least 12 km depth. About 12 km below the northern flank of the Alaska Range, we discovered a significant zone with low seismic velocities. This zone is believed to be related to magma and is located above the subducting Pacific Plate. We interpreted the anomaly as a magma reservoir beneath the volcanic gap, based on its tectonic and spatial relationship with nearby volcanoes.

1. Introduction

The south-central region of Alaska has a complex and active tectonic setting (Figure 1a). The low-angle flat subduction of the Pacific plate and the buoyant Yakutat slab transmit oblique convergence inland, causing counterclockwise rotation of south-central Alaska and orogenesis of the Alaska Range (Bemis et al., 2012; Freymueller et al., 2008; Haeussler, 2008). Most of the rotation is accommodated by the Denali fault (DF), a dextral strike-slip fault that accommodates about 20% of the convergence between the Pacific Plate/Yakutat terrane and the North American Plate (Matmon et al., 2006; Pavlis et al., 2004). The DF developed within the Alaska Range suture zone (SZ), the product of the oblique collision of allochthonous oceanic terranes in the south to the pericratonic terranes in the north (Ridgway et al., 2002).

The heterogeneous composition of the SZ crust reflects the nature of its origin. The metamorphic and sedimentary rocks of the SZ in Central Alaska, known as the Kahiltna assemblage, can be divided into northern and southern succession, with affinity to the Yukon Composite Terrane (YCT) (continental crust) and Wrangelia composite terrane (oceanic crust), respectively (Clautice, Newberry, Blodgett, et al., 2001; Clautice, Newberry,
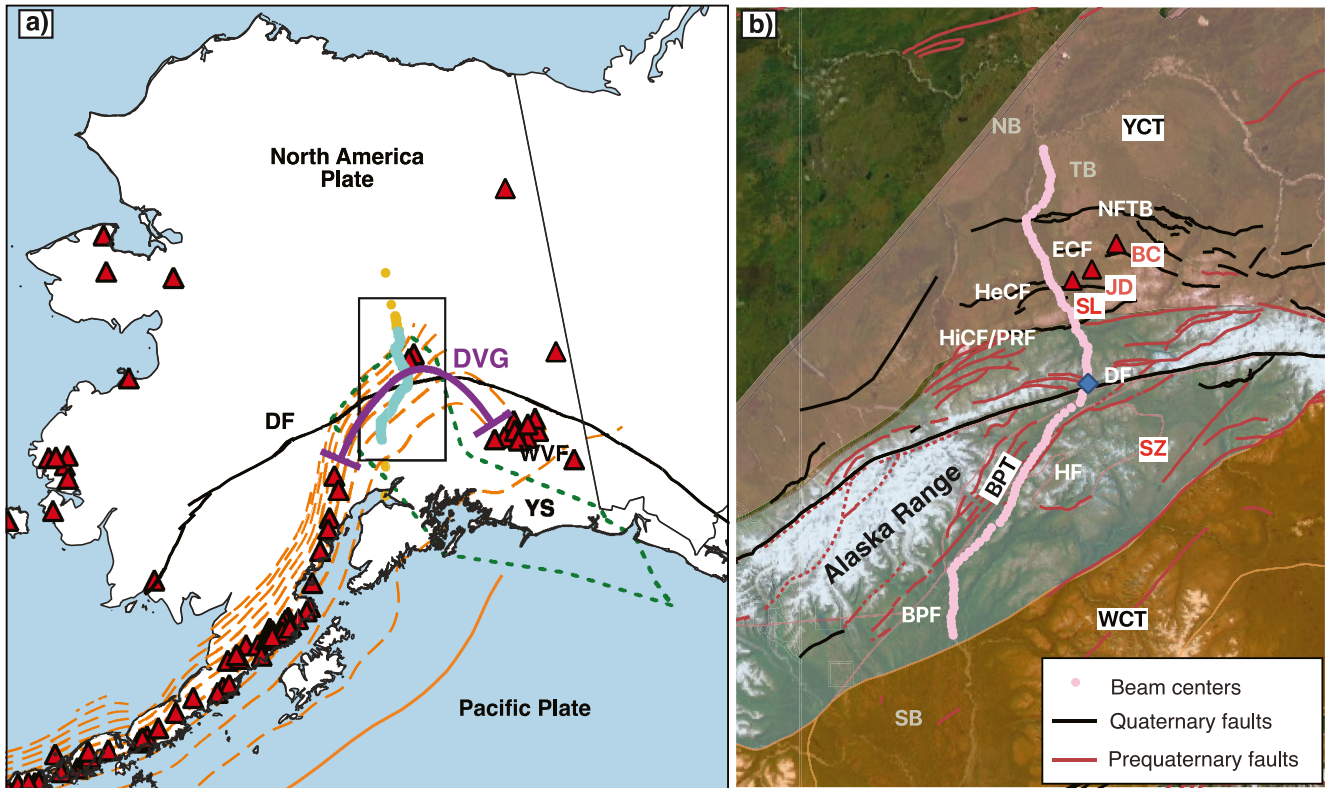
Figure 1. (a). Tectonic setting of Alaska. North America-Pacific convergent plate boundary (solid orange line) and slab depth contours (orange dashed lines) (Hayes et al., 2018). Other features include the geometry of the Yakutat Slab (YS) (green dashed outline) (Eberhart-Phillips et al., 2006), the Denali fault (DF) (black line), the Wrangell Volcanic Field (WVF), volcanoes (red triangles), nodal stations (cyan circles), broadband stations (yellow circles) used in this study. The purple line denotes the extension of the Denali Volcanic Gap (DVG). The black rectangle denotes the location of the right inset. (b). Location of the imaged region. Beam centers (light pink circles: 106 total), volcanoes (red triangles), Quaternary faults (black lines) (Koehler et al., 2013), and pre-Quaternary faults (red lines) (Koehler et al., 2012). The blue diamond identifies the beam used as an example in Figures 3–5, 7³⁻⁵, and 8. The gray labels are the major basins mentioned in the text: Susitna basin (SB), Nenana basin (NB), and Tanana basin (TB). The white labels are faults mentioned in the text: Broad Pass fault (BPF), Hurricane fault (HF), Denali fault (DF), Hines Creek fault/Parks Road fault (HiCF/PRF), Healy Creek Fault (HeCF), Ealy Creek fault (ECF), Northern Foothills Thrust Belt (NFTB). The red labels are volcanic features mentioned in the text: Jumbo Dome (JB), Buzzard Creek (BC), and Sugar Loaf Mountain (SL). The black labels are the Broad Pass Terrane (BPT), Wrangellia Composite Terrane (WTC, orange), suture zone (SZ, light blue), and the Yukon Composite Terrane (YCT, pink).

Pinney, et al., 2001; Hampton et al., 2010) (Figure 1). Both Kahlitna successions have rocks from volcanism and intrusions from the subduction-related arc and collisional magmatism (Romero et al., 2020); some of these rocks form the Broad Pass Terrane (BPT) (Clautice, Newberry, Blodgett, et al., 2001; Clautice, Newberry, Pinney, et al., 2001). The terranes north of the SZ are commonly referred to as the YCT, consisting of metamorphosed rocks of the former continental margin (Ridgway et al., 2002). The Hines Creek fault (HiCF), which likely extends to the bottom of the crust, is the northern margin of the SZ (Brennan et al., 2011) separating the accreted terranes to the south and the former continental margin to the north (Ridgway et al., 2007). Recent studies of the HiCF have shown the lack of lateral offsets on the fault while noting some near-vertical offsets (Bemis et al., 2012, 2015), in contrast to more than 480 km of dextral displacement of the DF (Waldien et al., 2021). The trace of the DF follows the Alaska Range and SZ (Haeussler, Matmon, et al., 2017).

Despite the active subduction of the Pacific-Yakutat slab beneath the area (Martin-Short et al., 2018), low volcanic activity is present within the Denali Volcanic Gap (DVG), a ~400 km region separating the active volcanism of the Aleutian Arc to the west and the Wrangell volcanoes to the east (Figure 1a). Whereas volcanic gaps are not unique to the Alaska subduction zone (e.g., Peru, Chile, Nankai, New Guinea) (Gutscher, Maury, et al., 2000), the DVG's origin remains enigmatic. Gutscher, Spakman, et al. (2000) argue that a low-angle flat subduction can interrupt mantle flow and inhibit arc volcanism. Chuang et al. (2017) propose that fluids are confined to only the uppermost part of the Yakutat crust, leading to an early release of fluids and a relatively anhydrous slab. Rondenay et al. (2010) propose the slab is generating melt but suggest the magmatic material does not rise to

the surface but accumulates at the top of the mantle wedge. Alternatively, the melt might be accumulating in the crust, where the compressional stress or structures in the Alaska Range impede magma upwelling (McNamara & Pasayanos, 2002).

North of the DF, there are two isolated contemporary volcanic bodies and one fossilized volcanic vent. The Buzzard Creek (BC) maars consist of two craters, dated at ca. 10 ka with basalt composition similar to the volcanoes in the eastern Aleutian Arc and the Wrangell Volcanic Field (WVF) (Albanese, 1980; Andronikov & Mukasa, 2010; Nye et al., 2018; Wood & Kienle, 1990). The Jumbo Dome Volcano, south of the BC maars, is a hornblende andesite dome (Cameron et al., 2015) dated at ca. 1 Ma (Athey et al., 2006) and composition similar to the adakite geochemical signature common in Wrangell arc lavas (Brueseke et al., 2019). South of the Jumbo Dome is Sugar Loaf Mountain, a fossilized volcanic vent with rhyolite and andesite composition (Albanese, 1980; Cameron et al., 2015; Reger, 1980). It is worth noting that the depth of the subducted slab beneath these volcanic bodies is ~100 km (Hayes et al., 2018), consistent with the global observations of slab-generating arc volcanism (Syracuse & Abers, 2006) independent of the thermal state of the slabs (Wada & Wang, 2009). The compositions of these bodies are similar to the volcanoes in the eastern Aleutian Arc and the western WVF, and the depth of the slab is ideal for arc volcanism, and therefore it is natural to consider an association with subduction (Albanese, 1980; Andronikov & Mukasa, 2010).

In this study, we use ambient seismic noise recorded by a 270 km long linear dense seismic array and image the 2D crustal structure down to 16 km depth across the Alaska Range. Leveraging the dense station coverage, our shear velocity image has a superior resolution compared with previous studies along the same profile in regional and continental studies using broadband stations (A. A. Allam et al., 2017; Berg et al., 2020; Eberhart-Phillips et al., 2006; Martin-Short et al., 2018; Rondenay et al., 2010; Y. Wang & Tape, 2014; Ward & Lin, 2018; X. Yang & Gao, 2020). The new model reveals detailed crustal features that were not imaged before, including a prominent middle crust low-velocity anomaly beneath the northern flank of the Alaska Range likely related to the magmatism associated with the DVG.

2. Data and Methodology

2.1. Data

In this study, we used ambient noise data from a semi-linear temporal nodal deployment and a handful of permanent stations installed along Parks Highway in South-Central Alaska (Figure 1). The temporal array consisted of 306 three-component 5 Hz geophones deployed from late February to early April in 2019 with a 1 km interstation distance (A. Allam et al., 2019). The southern end of the array is north of Anchorage near the town of Talkeetna, and the northern end is west of Fairbanks in the town of Nenana. To increase the number of measurements at the nodal stations, we use several existing broadband stations along the line as virtual sources and extend the array north and south, including seven stations from the FLATS array (2014–2019: Tape et al., 2018).

2.2. Ambient Noise Cross-Correlation

To calculate the three-component ambient noise cross-correlation, we follow Y. Wang, Allam, and Lin (2019). First, we remove the instrument response of all the stations, cut the data into 10-min segments, and whiten the three-component data simultaneously in the frequency domain based on the vertical spectrum. We then compute the nine-component cross-correlations between each station pair. Before stacking all the time windows, we normalize the multi-component cross-correlations by the maximum amplitude of the vertical-vertical component. For periods between 4 and 10 s, clear Rayleigh wave moveout can be observed in the cross-correlation record sections (e.g., Figure 2). The asymmetry of the cross-correlations indicates that the noise wavefield is dominantly propagating toward the north. Despite the inhomogeneous source distribution, the clear Rayleigh wave moveout suggests the noise wavefield is likely semi-diffusive and satisfies stationary phase approximation (Lin et al., 2008; Snieder, 2004; Y. Yang & Ritzwoller, 2008).

2.3. Rayleigh Phase Velocity and Ellipticity

We use beamforming (slant-stacking; Y. Wang, Allam, & Lin, 2019; Wells et al., 2022) to enhance the Rayleigh wave signals and to simultaneously determine location-dependent Rayleigh wave phase velocities (Figure 3) and
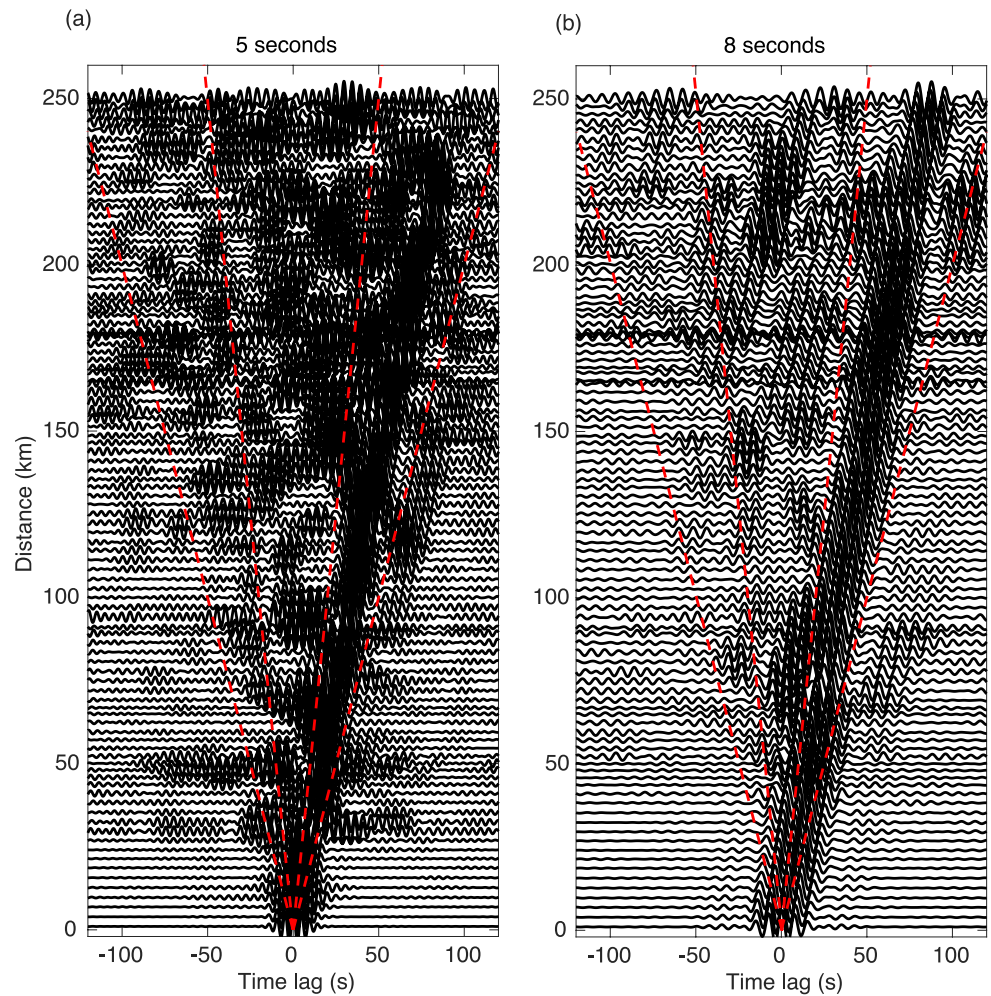
Figure 2. Example of noise cross-correlation record sections calculated for the vertical-vertical (ZZ) component between the southernmost nodal station (1001) and all the receiver stations filtered around (a) 5 s and (b) 8 s. Red dashed lines illustrate the reference velocity of 2 and 5 km/s. The higher amplitudes with positive time lags indicate that the noise is coming from the south of the array.

Rayleigh wave ellipticity or horizontal-to-vertical amplitude ratios (*H/V* ratio; Figure 4). The method determines surface wave properties at the receiver beam center, one source station at a time, by using cross-correlations between the source station and all receiver stations within the receiver beam. This is slightly different from the double beamforming technic (i.e., beams on both the source and receiver sides) presented by Y. Wang, Allam, and Lin (2019), Y. Wang, Lin, and Ward (2019), which works better when the array is closer to linear, and all ray paths are along the line. Compared to the traditional tomography method based on single station measurements, the beamforming approach has the advantage of improving signals that are close to or marginally above the noise level (e.g., Figure 2a). In this study, we include a total of 106 receiver beams in our analysis, that is one beam center per 0.02° latitude between 62.4°N and 64.5°N. The longitude of the beam center is determined by the averaged longitude of the two closest stations to that latitude. We use a 15 km beam diameter for the central part (between 63°N and 64.2°N), where coverage is best; in the northern and southern edges of the array (south of 63°N and north of 64.2°N), we use 30 km.

For each source-receiver pair, we first cut vertical-vertical (ZZ) and vertical-radial (ZR) cross-correlations based on a reference velocity of 7 km/s to remove early spurious arrivals (Y. Wang, Allam, & Lin, 2019; Y. Wang, Lin, & Ward, 2019; Yao et al., 2009). Next, we normalize the ZZ and ZR waveforms by the maximum ZZ amplitude. For each source station and all receiver stations within a receiver beam, we perform a grid search to find the best phase slowness that maximizes the envelope amplitude of the shifted and stacked ZZ waveforms (Figure 3).
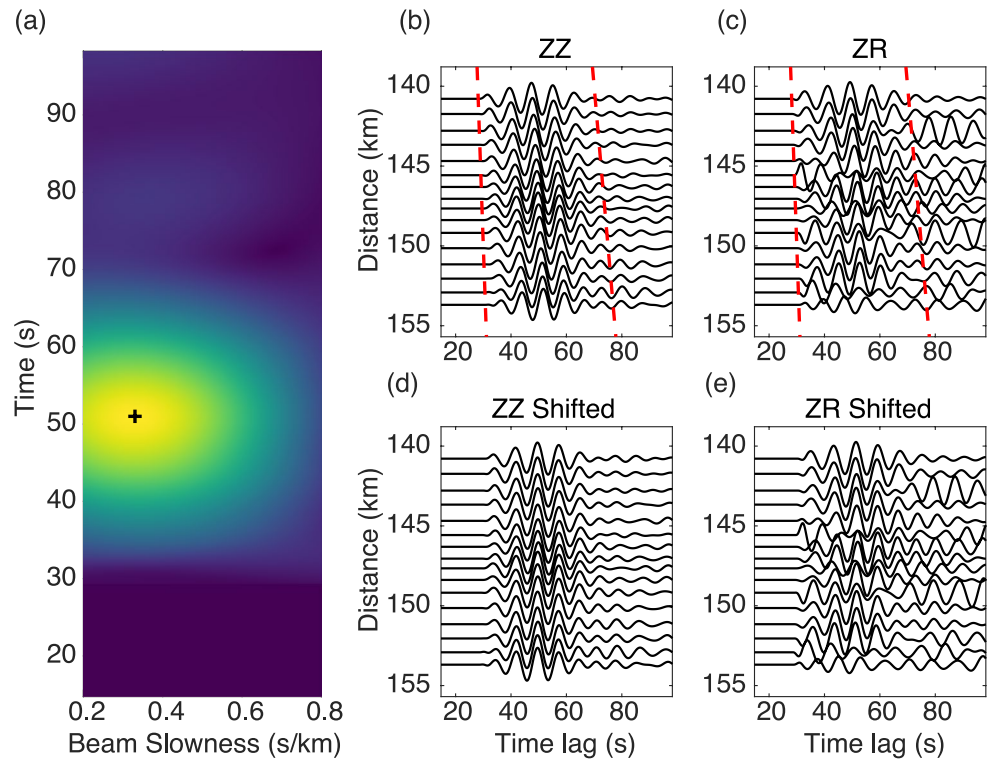
Figure 3. Example calculation of phase slowness based on slant stacking using the southernmost node as a source and beam 54 as a receiver (Figure 1). (a) Amplitude as a function of time and phase slowness of the shifted and stacked waveform envelope; the cross denotes the maximum amplitude of the grid search. (b) ZZ and (c) ZR component waveform before shifting; the red dashed lines denote reference velocity of 2 and 5 km/s (d) ZZ and (e) ZR component waveforms shifted by the maximum amplitude slowness.

In this procedure, only the correlation time lag corresponding to north propagation waves (the dominant noise direction) is used. A plane wave propagating in the great circle direction is assumed when calculating the shift time (Y. Wang, Allam, & Lin, 2019; Y. Wang, Lin, & Ward, 2019). To satisfy the far-field approximation, we only include cross-correlations with a distance larger than one wavelength (Liu et al., 2021), where the wavelength is estimated using a reference velocity of 4 km/s. While a stricter far-field criterion is sometimes desirable (e.g., three wavelengths; Lin et al., 2008), the one wavelength criterion used in this study is empirically determined to balance the number of measurements and the measurement uncertainty. To only keep the high-quality measurements, we further require a signal-to-noise ratio (SNR) greater than 5 on the stacked ZZ correlogram. The SNR is calculated based on the ratio between peak amplitude within the signal window (velocity between 1.5 and 5 km/s)
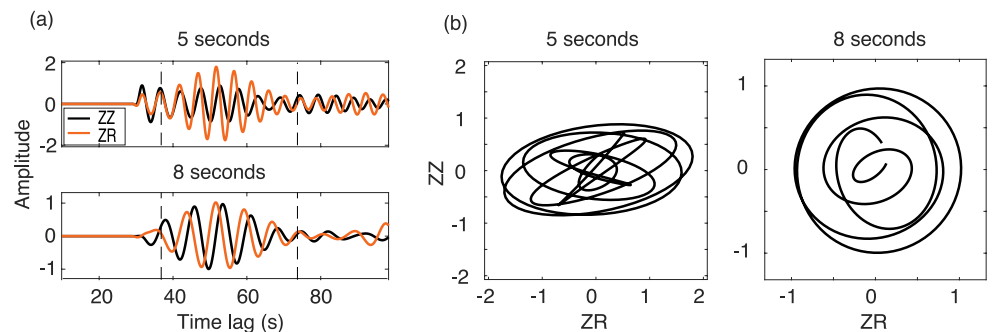

Figure 4. (a) ZZ (black) and ZR (orange) waveforms for (top) 5 s and (bottom) 8 s for the same source and receiver as in Figure 3. (b) Particle motion for waveforms in the left panel. For this example, the H/V measurements are 1.81 (5 s) and 1.03 (8 s).
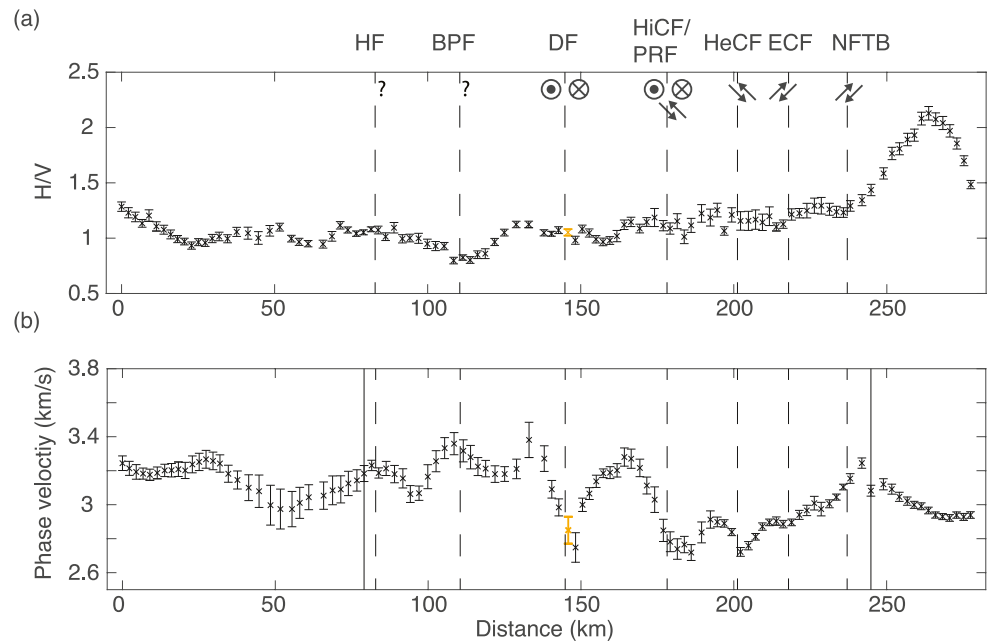
Figure 5. (a) H/V and (b) phase velocity measurements across the arrays at 8 s period. Error bars represent the uncertainties or standard deviation of the mean. Dashed lines represent the surface trace of the faults (Figure 1), solid lines represent the change from 30 km beams to 15 km beams, with 15 km beams used between about 63.0 and 64.25 latitude. The distance is a cumulative segmented distance connecting the 106 beams, starting with Beam 1 at 0 km in the south (Figure 1b). The orange measurement (Figure 1) and its uncertainty is the location—very close to the Denali fault—used as an example in Figures 7 and 8.

and root-mean-square (RMS) noise amplitude within the noise window, which is assigned as the end of the signal window to 20 s before the end of the correlogram.

The receiver beam phase slowness resolved using the ZZ component is then applied to also shift and stack the ZR waveforms. We use the ratio of the stacked ZZ and ZR maximum envelope amplitudes to determine the receiver beam Rayleigh wave H/V ratios (Figure 4). While H/V ratios can in principle also be measured using RZ and RR cross-correlations (Berg et al., 2018; Lin et al., 2014), these are not considered in this study because the RR cross-correlations are much noisier. In addition to requiring the SNR >5 for both stacked ZZ and ZR correlograms, two additional quality control criteria are used to remove less reliable H/V ratio measurements. First, we require that the ZZ and ZR phase travel time difference is smaller than one-eighth of a period, after accounting for the expected 90-degree phase shift (one-fourth of a period) between the vertical and radial components. Second, we require the ZZ and ZR group travel time difference to be smaller than one period to ensure we are measuring the same energy package for the two components.

For each receiver beam center location and each period, we determine the local Rayleigh wave phase slowness and H/V ratio and their uncertainties based on the mean and the standard deviation of the mean of all available measurements with different source stations. To remove outliers, we discard all measurements more than two standard deviations away from the mean and we also discard beams with less than 10 measurements in total. Figure 5 shows the resulting phase velocity and H/V ratio profiles across the entire linear array for 8 s period. The distance is measured along a segmented profile connecting each beam centers from south to north; it does not represent a cross-section along a great circle. For example, the end-to-end distance of 270 km is less than the along-road distance of 306 km between the most distant nodes. There are two reasons for this. First, the southernmost and northernmost beam centers are 8 km north and south of the southernmost and the northernmost node. The second reason is that simplifying the road geometry from 306 nodes to 106 beams can result in a loss of intricate curves and bends. Figure 6 summarizes the results for all periods and the corresponding uncertainty, where white patches represent situations where insufficient measurements (<10) passed the selection criteria imposed.
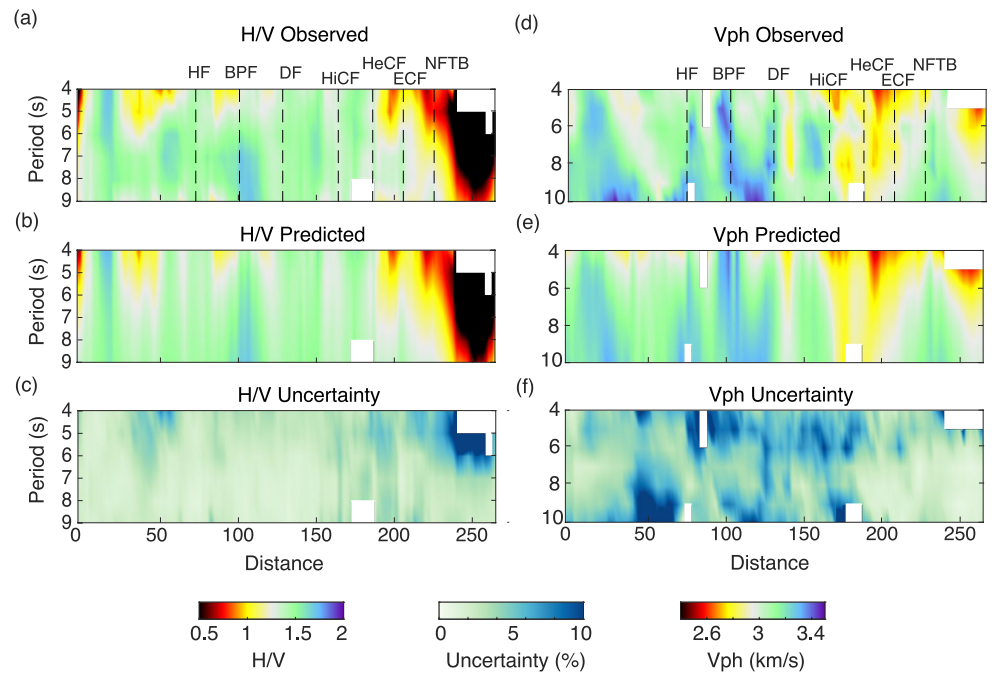
Figure 6. Measured *H/V* (a) and phase velocity (d). Predicted *H/V* (b) and phase velocity (e). Uncertainty of *H/V* (c) and phase velocity (f). These measurements are used in combination with the depth sensitivity functions in Figure 8 to generate the 2D V_s models in Figure 9. The fault abbreviations are identified in Figure 1.

2.4. MCMC Joint Inversion

We jointly invert Rayleigh wave phase dispersion and *H/V* ratio measurements at each location using a 1-D Markov Chain Monte Carlo (MCMC) method to resolve shear wave velocity (V_s) structure in the crust (Figure 7; Berg et al., 2020; Liu et al., 2021; Shen & Ritzwoller, 2016). The complementary sensitivity of Rayleigh wave phase velocities and *H/V* ratios (Figure 8) allows the crustal structure to be resolved from the surface to 16 km. We parametrize the V_s model to include a linearly increasing sedimentary layer (0–4 km thickness) and with the rest of the crust (down to 30 km) described by four cubic B-splines (Table 1). We use the Brocher (2005) empirical relationships to determine V_p and densities based on V_s. We use a 1-D V_s model extracted from a global V_s model (Shapiro & Ritzwoller, 2002) as the starting reference model of the inversion.

To fully explore the model space, we allow the MCMC inversion to search for V_s velocities that are up to ±3 km/s from the reference model. Two constraints are imposed to avoid unrealistic Earth models: (a) the V_s in the crust cannot be larger than 4.9 km/s, and (b) we require a positive jump in velocity at the base of the linear sedimentary layer. For each 1D inversion, we compute 3,000 randomly generated iterations with 12 jumps, generate more than 30,000 models, and accept only models within 1.5 times the minimum misfit. We average all the accepted models to obtain the final averaged model (Figure 7a). Only the top 16 km of the model is considered robust based on the sensitivity kernels of 4–10 s period Rayleigh wave measurements (Figure 8). All the piecewise continuous 1-D models are connected to construct the final 2-D V_s model across the array (Figure 9).

3. Results

3.1. Ellipticity and Phase Velocity Results

The resulting phase velocity profile (Figure 6d) reveals HiCF/PRF as an apparent boundary between faster velocities in the south and slower velocities in the north. The faster velocities in the south are mostly continuous in the 8–10 s range, sensitive to structure in the middle crust (Figure 8b), where small-scale variations between 3.0 and 3.4 km/s are observed for shorter periods. The DF emerges as a prominent localized low-velocity anomaly down to ~8 s period. For the northern half of the profile, there are three distinct short-period low-velocity anomalies: centered at the HiCF/PRF, bounded by the Healy Creek Fault (HeCF) and the Ely Creek fault (ECF), and north
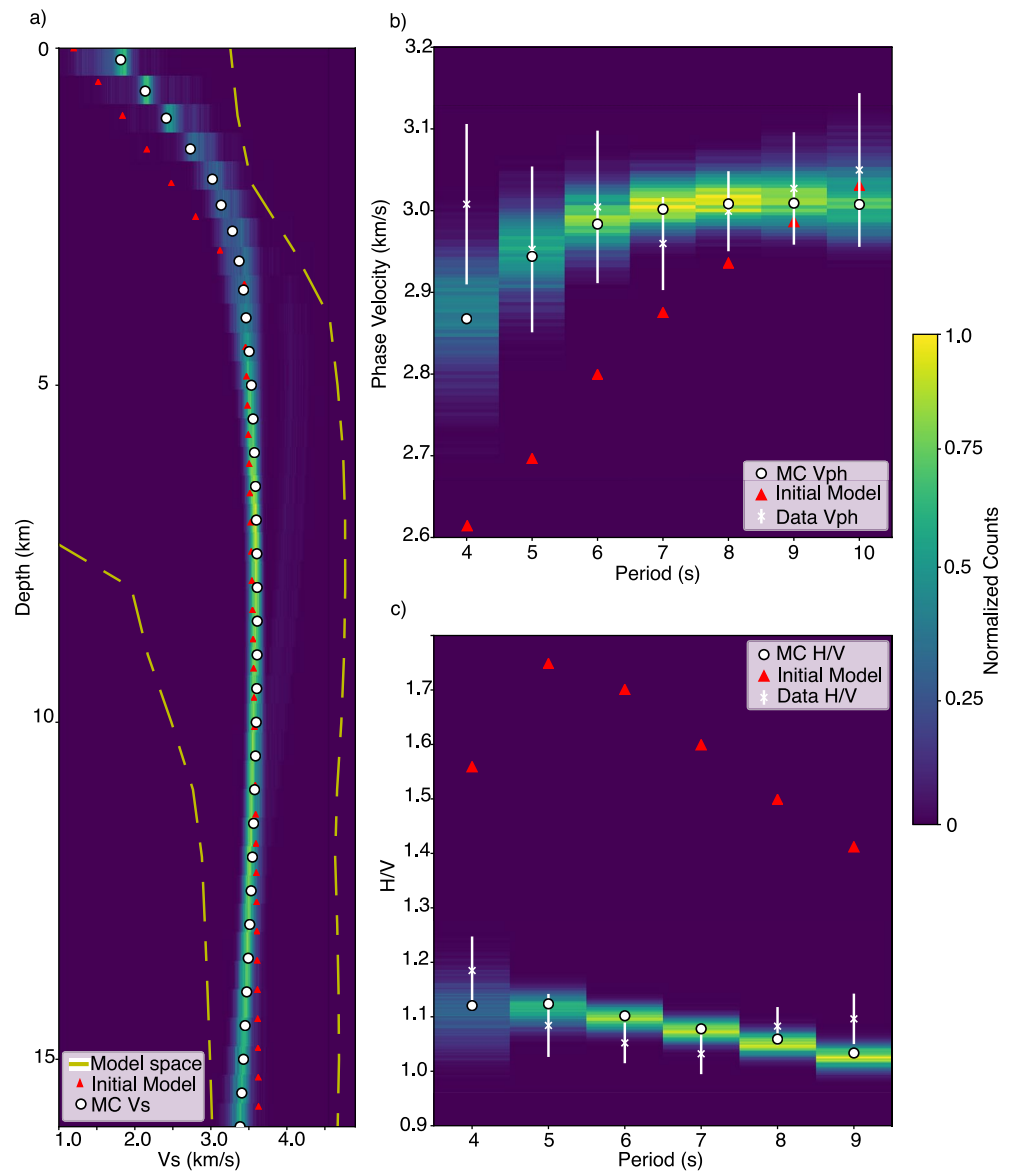
Figure 7. Example of Markov Chain Monte Carlo joint inversion for a 1-D V_s model at a location close to the Denali fault (Figure 5, orange marker), with 4410 models accepted. (a) Shear wave velocity versus depth showing the initial model (red triangles), the model space (dashed yellow lines), posterior model density (background color), and final mean model (white dots). (b) Rayleigh wave phase velocity dispersion measurements with its uncertainties from this study (white crosses with error bars) and predicted dispersion curves from the starting model (red triangles), posterior model density (background color), and final mean model (white dots). (c) Same as panel (b) but for Rayleigh H/V ratios.

of the Northern Foothills Thrust Belt (NFTB). The uncertainty on the measurements shows larger uncertainties for shorter periods (4–6 s) than for longer periods (7–10 s), likely due to stronger heterogeneity and wavefield complexity, such as multipathing or scattering. However, most uncertainties of the measurements are below 5%.

The resulting H/V ratio profile (Figure 6a) reveals structures distinct from the phase velocity profile, as H/V ratios are most sensitive to shallow crustal structure (Figure 8a; Lin et al., 2012). The observation of a high and low H/V ratio represents a large and small shallow velocity contrast/gradient, respectively, common for sedimentary basins and mountain ranges. There are several areas of high H/V ratios in the resulting profile. The highest H/V ratios are measured in the northern end of the array, bounded by the NFTB in the south. South of the NFTB and north of the HeCF, there are two different high H/V areas separated by the ECF. The other high H/V area is near the southern end of the profile. Unlike the phase velocity profile, we see no evidence of major fault zones in our
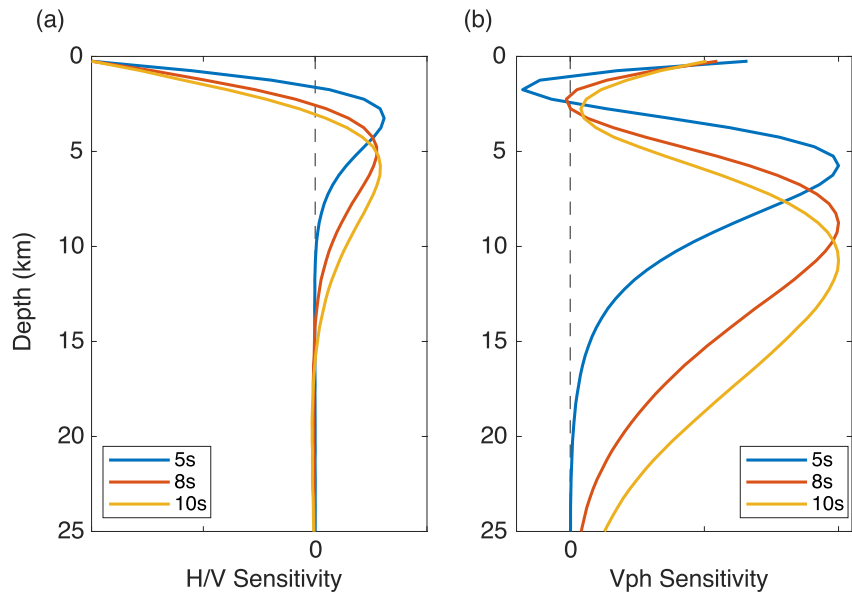
Figure 8. Example sensitivity kernels to changes in V_s at depth. (a) H/V and (b) phase velocity sensitivity kernels for a location near the Denali fault (Figure 5, orange marker) at three different periods calculated based on the inverted shear-wave velocity model.

ellipticity measurements. Besides elevated uncertainties near the northern edge coinciding with the higher H/V ratios, the H/V measurements mostly have uncertainty values below 5%.

3.2. Shear Wave Velocity Model

The shallow and deeper structures of the inverted shear velocity model (Figures 9a and 9b), in general, agree well with the pattern of the input H/V ratio and phase velocity profiles, with the predicted phase velocity and H/V ratio profiles in good agreement with the observed profiles (Figure 6). In the uppermost crust, major sedimentary structures with $V_s < 1.8$ km/s are observed, including the Susitna basin (SB)/Broad Pass (Figure 1) in the south, the Northern flank of the Alaska Range, and the Tanana basin (TB) in the north. Susitna basin is a Holocene basin connecting to the narrow Broad Pass and bounded by DF to the north. The Broad Pass slow anomaly is segregated by the inferred Hurricane fault (HF) and Broad Pass fault (BPF) locations. The Northern flank of the Alaska Range is the wedge-top depozone of the NFTB (Ridgway et al., 2007), and the slow anomaly is bounded and segregated by HeCF, ECF, and NFTB. North of NFTB, extremely slow V_s velocity (<1 km/s) is observed within the TB, which is a continental foreland basin covered by Holocene alluvial, fluvial, and lacustrine deposits.

Table 1
Prior Distributions in Joint Inversion

Parameters	Range
Sedimentary layer thickness	$2 \pm 2m0$ (km)
Sedimentary layer Vsv (top and bottom)	$m0 \pm 3.0$ (km/s)
Crust b-spline coefficients (4 total)	$m0 \pm 3.0$ (km/s)

Note. All parameters (left column), (right column) the ranges explored with $m0$ corresponding to the starting model variable's associated value.

Few major surface fault traces appear to extend deeper down and correlate with deeper crustal V_s structure (Figure 9b). Between 8 and 16 km depth, crustal velocity is generally slower north of the HiCF/PRF, presumably corresponding to the pericratonic YCT. A prominent low V_s anomaly (<3.2 km/s) bounded by HiCF/PRF and ECF is observed, which trends shallower around HeCF beneath Jumbo Dome (JB) and BC volcanic structure. The location of this slow anomaly also coincides with where the subducted Pacific-Yakutat slab steepened and deepened below 100 km depth (Figure 9d; Hayes et al., 2018). The overall faster structure south of HiCF/PRF is corresponding to the heterogenous SZ. The DF emerged as a narrow vertical slow anomaly down to ~12 km depth. A sharp velocity change is observed across the BPF although the nature of the velocity contrast is not so clear.
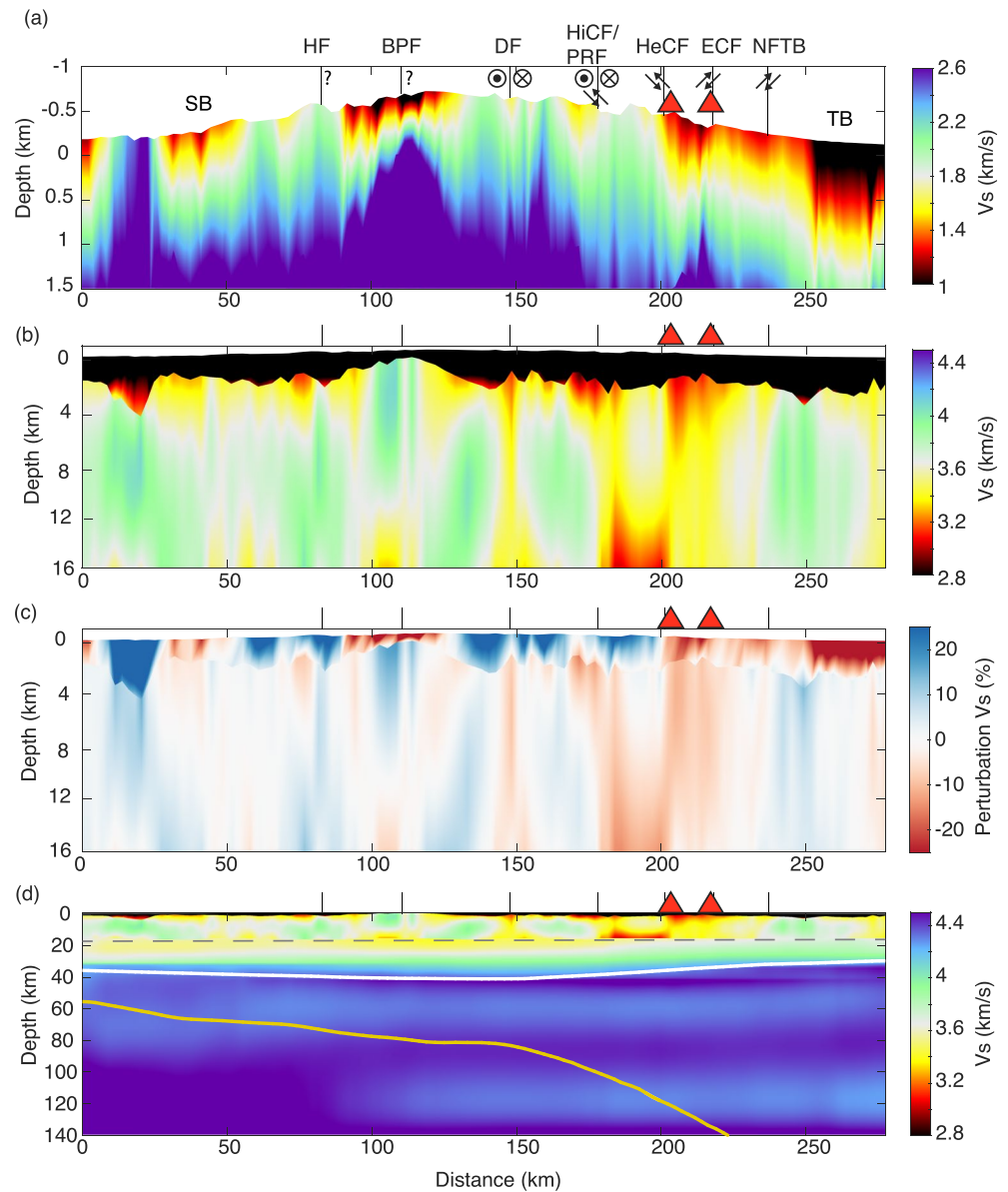
Figure 9. The inverted shear velocity (V_s, km/s) model. (a) Depth 0–1.5 km; vertical exaggeration 90×. (b) Depth 0–16 km; vertical exaggeration 15×. The locations of Susitna basin and Tanana basin are identified. Panel (c) same as panel (b) but for the V_s perturbation relative to the depth-averaged velocity. (d) The shear velocity model of this study (top 16 km above the dashed line and of Berg et al. (2020), 16–150 km). The white line is the Moho depth estimations from Miller & Moresi, 2018, and the yellow line is the depth of the slab from Slab 2.0 (Hayes et al., 2018); vertical exaggeration 2×. The fault abbreviations are identified in Figure 1.

4. Discussion

4.1. Magmatic Material Beneath the DVG

The low-velocity anomaly we observe beneath ~12 km depth between the HiCF/PRF and the ECF has not been previously reported either in regional studies (A. A. Allam et al., 2017; Eberhart-Phillips et al., 2006; Rondenay et al., 2010; Y. Wang & Tape, 2014; X. Yang & Gao, 2020) or in recent continental studies (Berg et al., 2020; Martin-Short et al., 2018; Ward & Lin, 2018). In the upper crust, this area, part of the DVG, contains the Northern Foothills fold-and-thrust belt that propagates northward. The interpreted location of the basal detachment of the fold-and-thrust belt here is around 7–8 km depth (Bemis & Wallace, 2007), right above the top of the observed

low-velocity anomaly. There are a few mechanisms that can result in an anomalous mid-crust low-velocity body, such as mineral composition, temperature, pressure, crack density, fluid content, or a combination of those factors.

First, the low-velocity anomaly might be related to fluids, either melt or fluid-filled cracks. The presence of the BC and Jumbo Dome could suggest that the slow velocity anomaly is related to magmatic/partial melt material rising from below and accumulating in the middle crust. Assuming V_s of 3.8 km/s (above the slow velocity zone) for the host rock, a ~15% melt percentage will be needed to reduce the V_s to ~3.2 km/s in the low-velocity zone, based on the modeling of preferred crystallographic orientation (Lee et al., 2017). Second, the low-velocity anomaly might correspond to a compositional change. North of the DF, the composition of the crust is mainly metasedimentary and metavolcanic rocks (Jones et al., 1983). Brennan et al. (2011) observed a negative anomaly in the receiver function and calculated a velocity ratio between *P*-wave and *S*-wave of ~1.6 for the area. The low ratio led to an interpretation of a crust with felsic composition and a juxtaposition of metamorphic rocks (greenschist over amphibolite), which Pavlis et al. (1993) suggest requires eliminating 10 km of the crustal column. Nevertheless, subsequent studies calculating V_p, V_s, and V_p/V_s have not observed this low ratio in the area, and they report a ratio higher than 1.75 (A. A. Allam et al., 2017). A negative receiver function anomaly from local models (A. A. Allam et al., 2017; Brennan et al., 2011) and a higher V_p/V_s (A. A. Allam et al., 2017) would favor the explanation of the low-velocity anomaly as fluid related instead of compositionally related. The geophysical data do not allow us to distinguish the type of fluids present in the low-velocity anomaly.

Although we do not have the sensitivity to resolve the lower crust and the upper mantle, our observation and the presence of recent basaltic volcanic activity (~10 ka) indicate that the mantle below the DVG is generating melt, and the material is reaching the surface. Our observation suggests that the magmatic material reaches the mid-crust beneath the northern flank of the Alaska Range, and it is stored around 12 km deep. We infer that the upward migration of the material is probably inhibited by the compressive stress from the shortening of the plate boundary transferred north of the DF to the fold-thrust belt, possibly sealing pathways in the crust, thereby hindering the movement of molten magma toward the surface (Bemis et al., 2015; McNamara & Pasayanos, 2002). Sporadically, the material may travel up to the detachment zone of the fold-thrust belt (Bemis & Wallace, 2007) and subsequently reach the surface through weak zones resulting from the fold and thrust system in the northern foothills of the Alaska Range.

4.2. Denali Fault and Other Faults

The DF is imaged in our results as a narrow, low-velocity zone at the same location as the surface trace of the fault (Figure 9b). Low-velocity zones are a common feature of seismogenic faults. They are created by breaking surrounding rock during coseismic shaking (Ben-Zion & Sammis, 2003). The velocity reduction at 3.5–10 km depth is around 15% from the surrounding crust. The narrow zone widens at depth (10–16 km) to the north. This type of geometry has been modeled for strike-slip faults (Finzi et al., 2009). In the 0–3.5 km depth range, the velocity is also slightly lower in the immediate vicinity of the DF compared to the surrounding structure, which could be related to the fault damage zone. Previous geophysical observations in the Eastern DF reported a maximum of 5 km wide composite damage zone attributed to the presence of several fault strands in a narrow area (Brocher et al., 2004) and geological observations indicate that the surface trace of the fault is in some locations <200 m wide (Benowitz et al., 2022). A damage zone structure typically ranges in size from hundreds of meters (Faulkner et al., 2011), to faults with damage zones that extend up to 1.5 km in width (Cochran et al., 2009). We cannot resolve smaller-scale structures (<5 km), given the limits on the resolution imposed by the beam size and the wavelength of the surface waves used in this research. The minimum resolution for this study, from ray theory, is half of the wavelength for each period (Z. Wang & Dahlen, 1995; Y. Wang, Allam, & Lin, 2019).

None of the other faults on this transect show a distinct fault zone structure near the surface (<1.5 km) or in the shallow- to mid-crust (1.5–16 km). There are two potential reasons for this. First, the previously discussed limitations on resolution could be a factor. Second, the presence of geological or tectonic boundaries associated with faults in the area could play a role. Larger velocity contrasts between different rock types may mask signals from smaller anomalies, in this case, a fault damage zone.

4.3. Suture Zone Northern Limit With the Yukon Terrane Boundary

We interpret the 10%–15% change of velocity at the HiCF/PRF as the northern edge of the SZ and the crustal boundary between the seismically faster SZ and the seismically slower YCT in the north (Figures 9b and 9c). The differences in seismic velocity between the north and the south can be explained by the geological history and the compositional change from oceanic to continental affinity crust from south to north (Hampton et al., 2010; Plafker & Berg, 1994; Ridgway et al., 2002). Our geophysical observation agrees with geological mapping interpreting the HiCF as the northern boundary of the SZ (Ridgway et al., 2002; Wahrhaftig et al., 1975). It would also agree with deeper observations of a sharp contrast in the Moho in the HiCF (Brennan et al., 2011; Miller & Moresi, 2018; Veenstra et al., 2006). Although it contrasts with previous local earthquake tomography results that identified the DF as the boundary of the SZ (A. A. Allam et al., 2017).

The fast velocity area bounded by the BPF to the north and the HF to the south could be related to the mafic and ultramafic rocks of the BPT underlining the Chulitna terrane (Jones et al., 1980) and corresponds with a positive magnetic anomaly (Burns et al., 2020). The BPF and the HF played an important role during the formation of the SZ in the Late Cretaceous with inferred strike-slip or thrust displacements (Clautice, Newberry, Blodgett, et al., 2001; Clautice, Newberry, Pinney, et al., 2001; Jones et al., 1980). They have been reactivated during the Holocene with a few kilometers of thrust displacement (Haeussler, Saltus, et al., 2017). The relationship between the terranes and the faults in the Broad Pass area is not fully understood (Clautice, Newberry, Blodgett, et al., 2001; Clautice, Newberry, Pinney, et al., 2001).

4.4. Sedimentary Basins

Our profile is bounded by two sedimentary basins: SB in the south and TB in the north. The southernmost low-velocity zone is located north of the main depocenter of SB, where exploration wells and seismic reflection lines show a sedimentary thickness of 4.5–5 km (Lewis et al., 2015; B. R. G. Stanley et al., 2013; R. G. Stanley et al., 2014). The geometry and depth of the observed low-velocity anomaly suggest an independent accumulation zone on the northern edge of the basin (Figures 9a and 9b). Sediment thickness information in the Broad Pass along the Chulitna River is scarce. The two low-velocity zones observed near the BPF (Figure 9a) agree with two distinct negative Bouguer gravity anomalies in the area (Meyer, 2005).

Our observation of thinning of the sedimentary layers from the HiCF/PRF toward the NFTB has also been reported using topography and structural geology observations (Bemis & Wallace, 2007). The low-velocity zones along the northern flank of the Alaska Range (Figures 9a and 9b) have been referred to as the wedge-top depozone of the TB in the fold and thrust system deformation (Ridgway et al., 2007). We identify two distinct anomalies in the Alaska Range. The southernmost anomaly, which we interpret as the foredeep basin (Ridgway et al., 2007), is deeper and has slower velocities at depth compared to the northern anomaly, which we interpret as the forebulge extending toward the Yukon-Tanana Uplands. In the northernmost anomaly, we observe a layer of 700–800 m with velocities lower than 1 km/s, and we observe velocities lower than 3 km/s up to 2.5–3 km depth.

Previous studies on the TB report depths of 1.5 km to the basement (Dixit & Hanks, 2021; Trop & Ridgway, 2007). The high velocity in the basement can be explained by the Yukon–Tanana Terrane schist underlying the basin (Dixit & Hanks, 2021). Our profile (Figure 1b) does not extend north beyond the town of Nenana into the Nenana basin (NB), where sediments up to 8 km deep have been interpreted from borehole data and seismic reflection data in the NB (Dixit & Hanks, 2021; Van Kooten et al., 2012).

5. Conclusions

This study presents a high-resolution 2-D shear-wave velocity profile of south-central Alaska across the DF and the Alaska Range. We measure Rayleigh wave H/V ratios and phase velocities calculated from ambient noise cross-correlation and invert for a shear velocity model through a joint MCMC inversion, which takes advantage of the complementary sensitivities of the measurements. We observe a mid-crust, low-velocity anomaly north of the HiCF and south of the Buzzard Creek and Jumbo Dome volcanoes. We favor the scenario that the LVZ is formed by fluids or melt material generated by the subducted slab being stored in the mid-crust. Within the top 5 km, our model delineates the SB, and the TB, south and north of the Alaska Range, respectively. We imaged the Alaska SZ in detail, including the northern limit at the HiCF, where seismic velocity in the north drops around 10%–15%.

We also imaged the DF as a narrow low-velocity anomaly extending to depths of 10–12 km. The new observation of the low-velocity anomaly beneath the DVG should spark future research to assess any possible hazard and to image the lateral limits of the anomaly. The use of other seismic and geophysical techniques with additional seismic deployments can help to measure the 3D extent and nature of the LVZ and is the target of future work.

Data Availability Statement

Data processing was performed with Seismic Analysis Code (SAC) and Matlab. Figure generation was performed in Matlab and Python 3.8. The nodal data is available on the Incorporated Research Institutions for Seismology (IRIS) database with DOI A. Allam et al. (2019) (https://doi.org/10.7914/SN/ZE_2019). Additional seismic data included broadband stations from the Alaska Earthquake Center (1987) (DOI: https://doi.org/10.7914/SN/AK), the Earthscope Transportable Array (2003) (DOI: https://doi.org/10.7914/SN/TA) and the FLATS array (Tape & West, 2014) (DOI: https://doi.org/10.7914/SN/XV_2014). The 2-D shear wave velocity model is available at https://doi.org/10.5281/zenodo.10257242.

References

Alaska Earthquake Center, University of Alaska Fairbanks. (1987). Alaska regional network [Dataset]. International Federation of Digital Seismograph Networks. https://doi.org/10.7914/SN/AK

Albanese, M. (1980). *The geology of three extrusive bodies in central Alaska Range* (Master thesis). University of Alaska Fairbanks.

Allam, A., Tape, C., & Ward, K. (2019). Node deployment along the intersection of the Denali Fault and Parks Highway [Dataset]. International Federation of Digital Seismograph Networks. https://doi.org/10.7914/SN/ZE_2019

Allam, A. A., Schulte-Pelkum, V., Ben-Zion, Y., Tape, C., Ruppert, N., & Ross, Z. E. (2017). Ten kilometer vertical Moho offset and shallow velocity contrast along the Denali fault zone from double-difference tomography, receiver functions, and fault zone head waves. In *Tectonophysics* (Vol. 721, pp. 56–69). Elsevier BV. https://doi.org/10.1016/j.tecto.2017.09.003

Andronikov, A. V., & Mukasa, S. B. (2010). 40Ar/39Ar eruption ages and geochemical characteristics of Late Tertiary to Quaternary intraplate and arc-related lavas in interior Alaska. *Lithos*, *115*(1–4), 1–14. https://doi.org/10.1016/j.lithos.2009.11.002

Athey, J., Newberry, R., Werden, M., Freeman, L., Smith, R., & Szumigala, D. (2006). Bedrock geologic map of the liberty Bell area, Fairbanks A-4 Quadrangle, Bonnifield mining district, Alaska. In *Report of investigation RI2006, 1.0.1*.

Bemis, S. P., Carver, G. A., & Koehler, R. D. (2012). The Quaternary thrust system of the northern Alaska Range. *Geosphere*, *8*(1), 196–205. https://doi.org/10.1130/GES00695.1

Bemis, S. P., & Wallace, W. K. (2007). Neotectonic framework of the north-central Alaska range foothills. *Special Paper of the Geological Society of America*, *431*(21), 549–572. https://doi.org/10.1130/2007.2431(21)

Bemis, S. P., Weldon, R. J., & Carver, G. A. (2015). Slip partitioning along a continuously curved fault: Quaternary geologic controls on Denali fault system slip partitioning, growth of the Alaska Range, and the tectonics of south-central Alaska. *Lithosphere*, *7*(3), 235–246. https://doi.org/10.1130/L352.1

Benowitz, J. A., Roeske, S. M., Regan, S. P., Waldien, T. S., Elliott, J. L., & O'Sullivan, P. B. (2022). Large-scale, crustal-block vertical extrusion between the Hines Creek and Denali faults coeval with slip localization on the Denali fault since ca. 45 Ma, Hayes Range, Alaska, USA. *Geosphere*, *18*(3), 1030–1054. https://doi.org/10.1130/ges02466.1

Ben-Zion, Y., & Sammis, C. G. (2003). Characterization of fault zones. *Pure and Applied Geophysics*, *160*(3), 677–715. https://doi.org/10.1007/PL00012554

Berg, E. M., Lin, F., Allam, A., Schulte-Pelkum, V., Ward, K. M., & Shen, W. (2020). Shear velocity model of Alaska via joint inversion of Rayleigh wave ellipticity, phase velocities, and receiver functions across the Alaska transportable array. *Journal of Geophysical Research: Solid Earth*, *125*(2), 1–22. https://doi.org/10.1029/2019JB018582

Berg, E. M., Lin, F. C., Allam, A., Qiu, H., Shen, W., & Ben-Zion, Y. (2018). Tomography of southern California via Bayesian joint inversion of Rayleigh wave ellipticity and phase velocity from ambient noise cross-correlations. *Journal of Geophysical Research: Solid Earth*, *123*(11), 9933–9949. https://doi.org/10.1029/2018JB016269

Brennan, P. R., Gilbert, H., & Ridgway, K. D. (2011). Crustal structure across the central Alaska Range: Anatomy of a Mesozoic collisional zone. *Geochemistry, Geophysics, Geosystems*, *12*(4), 52. https://doi.org/10.1029/2011GC003519

Brocher, T. M. (2005). Empirical relations between elastic wavespeeds and density in the Earth's crust. *Bulletin of the Seismological Society of America*, *95*(6), 2081–2092. https://doi.org/10.1785/0120050077

Brocher, T. M., Fuis, G. S., Lutter, W. J., Christensen, N. I., & Ratchkovski, N. A. (2004). Seismic velocity models for the Denali fault zone along the Richardson Highway, Alaska. *Bulletin of the Seismological Society of America*, *94*(6B), S85–S106. https://doi.org/10.1785/0120040615

Brueseke, M. E., Benowitz, J. A., Trop, J. M., Davis, K. N., Berkelhammer, S. E., Layer, P. W., & Morter, B. K. (2019). The Alaska Wrangell Arc:~ 30 Ma of subduction-related magmatism along a still active arc-transform junction. *Terra Nova*, *31*(1), 59–66. https://doi.org/10.1111/ter.12369

Burns, L. E., Graham, G. R. C., Barefoot, J. D., Woods, R.-E., & Pritchard, R. A. (2020). *Chulitna electromagnetic and magnetic airborne geophysical survey*. Alaska Division of Geological & Geophysical Surveys. https://doi.org/10.14509/30416

Cameron, C. E., Nye, C. J., Bull, K. F., & Woods, R.-E. (2015). *Jumbo Dome, Interior Alaska: Whole-rock, major- and trace-element analyses*. State of Alaska, Department of Natural Resources, Division of Geological & Geophysical Surveys. https://doi.org/10.14509/29520

Chuang, L., Bostock, M., Wech, A., & Plourde, A. (2017). Plateau subduction, intraslab seismicity, and the Denali (Alaska) volcanic gap. *Geology*, *45*(7), 647–650. https://doi.org/10.1130/G38867.1

Clautice, K. H., Newberry, R. J., Blodgett, R. B., Bundtzen, T. K., Gage, B. G., Harris, E. E., et al. (2001). *Bedrock geologic map of the Chulitna region, southcentral Alaska*. Alaska Division of Geological & Geophysical Surveys. https://doi.org/10.14509/2768

Clautice, K. H., Newberry, R. J., Pinney, D. S., Blodgett, R. B., Bundtzen, T. K., Gage, B. G., et al. (2001). *Geologic map of the Chulitna region, southcentral Alaska*. Alaska Division of Geological & Geophysical Surveys. https://doi.org/10.14509/2771

Cochran, E. S., Li, Y. G., Shearer, P. M., Barbot, S., Fialko, Y., & Vidale, J. E. (2009). Seismic and geodetic evidence for extensive, long-lived fault damage zones. *Geology*, *37*(4), 315–318. https://doi.org/10.1130/G25306A.1

Dixit, N. C., & Hanks, C. (2021). Basement structure and styles of active tectonic deformation in central interior Alaska. *Geosciences*, *11*(3), 1–28. https://doi.org/10.3390/geosciences11030127

Earthscope Transportable Array. (2003). USArray transportable array [Dataset]. International Federation of Digital Seismograph Networks. https://doi.org/10.7914/SN/TA

Eberhart-Phillips, D., Christensen, D. H., Brocher, T. M., Hansen, R., Ruppert, N. A., Haeussler, P. J., & Abers, G. A. (2006). Imaging the transition from Aleutian subduction to Yakutat collision in central Alaska, with local earthquakes and active source data. *Journal of Geophysical Research*, *111*(B11), B11303. https://doi.org/10.1029/2005JB004240

Faulkner, D. R., Mitchell, T. M., Jensen, E., & Cembrano, J. (2011). Scaling of fault damage zones with displacement and the implications for fault growth processes. *Journal of Geophysical Research*, *116*(B5), B05403. https://doi.org/10.1029/2010JB007788

Finzi, Y., Hearn, E. H., Ben-Zion, Y., & Lyakhovsky, V. (2009). Structural properties and deformation patterns of evolving strike-slip faults: Numerical simulations incorporating damage rheology. *Pure and Applied Geophysics*, *166*(10), 1537–1573. https://doi.org/10.1007/s00024-009-0522-1

Freymueller, J. T., Woodard, H., Cohen, S. C., Cross, R., Elliott, J., Larsen, C. F., et al. (2008). Active deformation processes in Alaska, based on 15 years of GPS measurements. In J. T. Freymueller, P. J. Haeussler, R. L. Wesson, & G. Ekström (Eds.), *Active tectonics and seismic potential of Alaska*. https://doi.org/10.1029/179GM02

Gutscher, M. A., Maury, R., Eissen, J. P., & Bourdon, E. (2000). Can slab melting be caused by flat subduction? *Geology*, *28*(6), 535–538. https://doi.org/10.1130/0091-7613(2000)28<535:CSMBCB>2.0.CO;2

Gutscher, M. A., Spakman, W., Bijwaard, H., & Engdahl, E. R. (2000). Geodynamics of flat subduction: Seismicity and tomographic constraints from the Andean margin. *Tectonics*, *19*(5), 814–833. https://doi.org/10.1029/1999TC001152

Haeussler, P. J. (2008). An overview of the neotectonics of interior Alaska: Far-field deformation from the Yakutat microplate collision. In J. T. Freymueller, P. J. Haeussler, R. L. Wesson, & G. Ekström (Eds.), *Active tectonics and seismic potential of Alaska*. https://doi.org/10.1029/179GM05

Haeussler, P. J., Matmon, A., Schwartz, D. P., & Seitz, G. G. (2017). Neotectonics of interior Alaska and the late Quaternary slip rate along the Denali fault system. *Geosphere*, *13*(5), 1445–1463. https://doi.org/10.1130/GES01447.1

Haeussler, P. J., Saltus, R. W., Stanley, R. G., Ruppert, N., Lewis, K., Karl, S. M., & Bender, A. (2017). The Peters Hills basin, a Neogene wedge-top basin on the Broad Pass thrust fault, south-central Alaska. *Geosphere*, *13*(5), 1464–1488. https://doi.org/10.1130/ges01487.1

Hampton, B. A., Ridgway, K. D., & Gehrels, G. E. (2010). A detrital record of Mesozoic island arc accretion and exhumation in the North American Cordillera: U-Pb geochronology of the Kahiltna basin, southern Alaska. *Tectonics*, *29*(4), TC4015. https://doi.org/10.1029/2009TC002544

Hayes, G. P., Moore, G. L., Portner, D. E., Hearne, M., Flamme, H., Furtney, M., & Smoczyk, G. M. (2018). Slab2, a comprehensive subduction zone geometry model. *Science*, *362*(6410), 58–61. https://doi.org/10.1126/science.aat4723

Jones, D. L., Silberling, N. J., Csejtey, B., Jr., Nelson, W. H., & Blome, C. D. (1980). Age and structural significance of ophiolite and adjoining rocks in the upper Chulitna district, south-central Alaska: US Geol. In *Survey professional paper* (p. 1121).

Jones, D. L., Silberling, N. J., Gilbert, W. J., & Coney, P. J. (1983). Tectono-stratigraphic map and interpretive bedrock geologic map of the Mount McKinley region, Alaska (no. 83-11).

Koehler, R. D., Burns, P. A. C., & Weakland, J. R. (2013). Digitized faults of the Neotectonic map of Alaska (Plafker and others, 1994). In R. D. Koehler (Ed.), *Quaternary faults and folds (QFF)* (Vol. 150, p. 1). Alaska Division of Geological & Geophysical Surveys Miscellaneous Publication. https://doi.org/10.14509/24791

Koehler, R. D., Farrell, R.-E., Burns, P. A. C., & Combellick, R. A. (2012). Quaternary faults and folds in Alaska: A digital database. In R. D. Koehler (Ed.), *Quaternary faults and folds (QFF), 1 sheet, scale 1:3,700,000* (Vol. 141, p. 31). Alaska Division of Geological & Geophysical Surveys Miscellaneous Publication. https://doi.org/10.14509/23944

Lee, A. L., Walker, A. M., Lloyd, G. E., & Torvela, T. (2017). Modeling the impact of melt on seismic properties during mountain building. *Geochemistry, Geophysics, Geosystems*, *18*(3), 1090–1110. https://doi.org/10.1002/2016GC006705

Lewis, K. A., Potter, C. J., Shah, A. K., Stanley, R. G., Haeussler, P. J., & Saltus, R. W. (2015). *Preliminary interpretation of industry two-dimensional seismic data from Susitna basin, south-central Alaska*. US Department of the Interior, US Geological Survey. https://doi.org/10.3133/ofr20151138

Lin, F.-C., Moschetti, M. P., & Ritzwoller, M. H. (2008). Surface wave tomography of the western United States from ambient seismic noise: Rayleigh and love wave phase velocity maps. *Geophysical Journal International*, *173*(1), 281–298. https://doi.org/10.1111/j.1365-246X.2008.03720.x

Lin, F.-C., Schmandt, B., & Tsai, V. C. (2012). Joint inversion of Rayleigh wave phase velocity and ellipticity using USArray: Constraining velocity and density structure in the upper crust. *Geophysical Research Letters*, *39*(12), L12303. https://doi.org/10.1029/2012GL052196

Lin, F. C., Tsai, V. C., & Schmandt, B. (2014). 3-D crustal structure of the western United States: Application of Rayleigh-wave ellipticity extracted from noise cross-correlations. *Geophysical Journal International*, *198*(2), 656–670. https://doi.org/10.1093/gji/ggu160

Liu, C. N., Lin, F. C., Huang, H. H., Wang, Y., Berg, E. M., & Lin, C. H. (2021). High-resolution 3-D shear wave velocity model of northern Taiwan via Bayesian joint inversion of Rayleigh wave ellipticity and phase velocity with Formosa array. *Journal of Geophysical Research: Solid Earth*, *126*(5), 1–18. https://doi.org/10.1029/2020JB021610

Martin-Short, R., Allen, R., Bastow, I. D., Porritt, R. W., & Miller, M. S. (2018). Seismic imaging of the Alaska subduction zone: Implications for slab geometry and volcanism. *Geochemistry, Geophysics, Geosystems*, *19*(11), 4541–4560. https://doi.org/10.1029/2018GC007962

Matmon, A., Schwartz, D. P., Haeussler, P. J., Finkel, R., Lienkaemper, J. J., Stenner, H. D., & Dawson, T. E. (2006). Denali fault slip rates and Holocene–Late Pleistocene kinematics of central Alaska. *Geology*, *34*(8), 645–648. https://doi.org/10.1130/G22361.1

McNamara, D. E., & Pasayanos, M. E. (2002). Seismological evidence for a sub-volcanic arc mantle wedge beneath the Denali volcanic gap, Alaska. *Geophysical Research Letters*, *29*(16), 1814. https://doi.org/10.1029/2001GL014088

Meyer, J. F. (2005). *Principal facts for gravity data collected in the northern Susitna Basin area, southcentral Alaska*. Alaska Department of Natural Resources, Division of Geological & Geophysical Surveys. https://doi.org/10.14509/7186

Miller, M. S., & Moresi, L. (2018). Mapping the Alaskan Moho. *Seismological Research Letters*, *89*(6), 2430–2436. https://doi.org/10.1785/0220180222

Nye, C. J., Beget, J. E., Layer, P. W., Mangan, M. T., McConnell, V. S., McGimsey, R. G., et al. (2018). *Geochemistry of some quaternary lavas from the Aleutian arc and Mt. Wrangell*. Alaska Division of Geological & Geophysical Surveys. https://doi.org/10.14509/29843

Pavlis, T. L., Picornell, C., Serpa, L., Bruhn, R. L., & Plafker, G. (2004). Tectonic processes during oblique collision: Insights from the St. Elias orogen, northern North American Cordillera. *Tectonics*, *23*(3), TC3001. https://doi.org/10.1029/2003TC001557

Pavlis, T. L., Sisson, V. B., Foster, H. L., Nokleberg, W. J., & Plafker, G. (1993). Mid-cretaceous extensional tectonics of the Yukon-tanana terrane, trans-Alaska crustal transect (TACT), east-central Alaska. *Tectonics*, *12*(1), 103–122. https://doi.org/10.1029/92TC00860

Plafker, G., & Berg, H. C. (1994). Overview of the geology and tectonic evolution of Alaska. In G. Plafker & H. C. Berg (Eds.), *The geology of Alaska: Volume G-1*. Geological Society of America. https://doi.org/10.1130/DNAG-GNA-G1.989

Reger, R. D. (1980). Short notes on Alaskan geology: 1979–1980. *Angewandte Chemie International Edition*, *6*(11), 951–952. https://doi.org/10.14509/417

Ridgway, K. D., Thoms, E. E., Layer, P. W., Lesh, M. E., White, J. M., & Smith, S. V. (2007). Neogene transpressional foreland basin development on the north side of the central Alaska range, Usibelli group and Nenana gravel, Tanana Basin. *Special Paper of the Geological Society of America*, *431*(20), 507–547. https://doi.org/10.1130/2007.2431(20)

Ridgway, K. D., Trop, J. M., Nokleberg, W. J., Davidson, C. M., & Eastham, K. R. (2002). Mesozoic and Cenozoic tectonics of the eastern and central Alaska Range: Progressive basin development and deformation in a suture zone. *GSA Bulletin*, *114*(12), 1480–1504. https://doi.org/10.1130/0016-7606(2002)114<1480:MACTOT>2.0.CO;2

Romero, M. C., Ridgway, K. D., & Gehrels, G. E. (2020). Geology, U-Pb geochronology, and Hf isotope geochemistry across the Mesozoic Alaska Range suture zone (south-central Alaska): Implications for Cordilleran collisional processes and tectonic growth of North America. *Tectonics*, *39*(3), e2019TC005946. https://doi.org/10.1029/2019TC005946

Rondenay, S., Montési, L. G. J., & Abers, G. A. (2010). New geophysical insight into the origin of the Denali volcanic gap. *Geophysical Journal International*, *182*(2), 613–630. https://doi.org/10.1111/j.1365-246X.2010.04659.x

Shapiro, N. M., & Ritzwoller, M. H. (2002). Monte-Carlo inversion for a global shear-velocity model of the crust and upper mantle. *Geophysical Journal International*, *151*(1), 88–105. https://doi.org/10.1046/j.1365-246X.2002.01742.x

Shen, W., & Ritzwoller, M. H. (2016). Crustal and uppermost mantle structure beneath the United States. *Journal of Geophysical Research: Solid Earth*, *121*(6), 4306–4342. https://doi.org/10.1002/2016jb012887

Snieder, R. K. (2004). Extracting the Green's function from the correlation of coda waves: A derivation based on stationary phase. *Physical Review E*, *69*(4), 046610. https://doi.org/10.1103/PhysRevE.69.046610

Stanley, B. R. G., Haeussler, P. J., Benowitz, J. A., Goodman, D. K., Ravn, R. L., Shellenbaum, D. P., et al. (2013). New stratigraphic revelations in the subsurface Susitna basin, south-central Alaska, from recent isotopic and biostratigraphic results. In *Geological society of America abstracts with programs* (Vol. 45, p. 69). https://doi.org/10.14509/26887

Stanley, R. G., Haeussler, P. J., Benowitz, J. A., Lewis, K. A., Shellenbaum, D. P., Richard, W., et al. (2014). Tectonic implications of new geological and geophysical results from the Susitna basin, south-central Alaska. In *Search and discovery article, 10608*.

Syracuse, E. M., & Abers, G. A. (2006). Global compilation of variations in slab depth beneath arc volcanoes and implications. *Geochemistry, Geophysics, Geosystems*, *7*(5), Q05017. https://doi.org/10.1029/2005GC001045

Tape, C., Holtkamp, S., Silwal, V., Hawthorne, J., Kaneko, Y., Ampuero, J. P., et al. (2018). Earthquake nucleation and fault slip complexity in the lower crust of central Alaska. *Nature Geoscience*, *11*(7), 536–541. https://doi.org/10.1038/s41561-018-0144-2

Tape, C., & West, M. E. (2014). Fault locations and Alaska tectonics from seismicity [Dataset]. International Federation of Digital Seismograph Networks. https://doi.org/10.7914/SN/XV_2014

Trop, J. M., & Ridgway, K. D. (2007). Mesozoic and Cenozoic tectonic growth of southern Alaska: A sedimentary basin perspective. *Special Paper of the Geological Society of America*, *431*(04), 55–94. https://doi.org/10.1130/2007.2431(04)

Van Kooten, G. K., Richter, M., & Zippi, P. A. (2012). Alaska's interior rift basins: A new Frontier for discovery. *Oil and Gas Journal, Exploration and Development*. https://doi.org/10.1139/cjes-2015-0138

Veenstra, E., Christensen, D. H., Abers, G. A., & Ferris, A. (2006). Crustal thickness variation in south-central Alaska. *Geology*, *34*(9), 781–784. https://doi.org/10.1130/G22615.1

Wada, I., & Wang, K. (2009). Common depth of slab-mantle decoupling: Reconciling diversity and uniformity of subduction zones. *Geochemistry, Geophysics, Geosystems*, *10*(10), Q10009. https://doi.org/10.1029/2009GC002570

Wahrhaftig, C., Turner, D. L., Weber, F. R., & Smith, T. E. (1975). Nature and timing of movement on Hines Creek strand of Denali fault system, Alaska. *Geology*, *3*(8), 463–466. https://doi.org/10.1130/0091-7613(1975)3<463:NATOMO>2.0.CO;2

Waldien, T. S., Roeske, S. M., Benowitz, J. A., Twelker, E., & Miller, M. S. (2021). Oligocene-Neogene lithospheric-scale reactivation of Mesozoic terrane accretionary structures in the Alaska Range suture zone, southern Alaska, USA. *GSA Bulletin*, *133*(3–4), 691–716. https://doi.org/10.1130/B35665.1

Wang, Y., Allam, A., & Lin, F. C. (2019). Imaging the fault damage zone of the san Jacinto fault near Anza with ambient noise tomography using a dense nodal array. *Geophysical Research Letters*, *46*(22), 12938–12948. https://doi.org/10.1029/2019GL084835

Wang, Y., Lin, F. C., & Ward, K. M. (2019). Ambient noise tomography across the Cascadia subduction zone using dense linear seismic arrays and double beamforming. *Geophysical Journal International*, *217*(3), 1668–1680. https://doi.org/10.1093/gji/ggz109

Wang, Y., & Tape, C. (2014). Seismic velocity structure and anisotropy of the Alaska subduction zone based on surface wave tomography. *Journal of Geophysical Research: Solid Earth*, *119*(12), 8845–8865. https://doi.org/10.1002/2014jb011438

Wang, Z., & Dahlen, F. A. (1995). Validity of surface-wave ray theory on a laterally heterogeneous earth. *Geophysical Journal International*, *123*(3), 757–773. https://doi.org/10.1111/j.1365-246X.1995.tb06888.x

Ward, K. M., & Lin, F. C. (2018). Lithospheric structure across the Alaskan cordillera from the joint inversion of surface waves and receiver functions. *Journal of Geophysical Research: Solid Earth*, *123*(10), 8780–8797. https://doi.org/10.1029/2018jb015967

Wells, D., Lin, F., Pankow, K., Baker, B., & Bartley, J. (2022). Combining dense seismic arrays and broadband data to image the subsurface velocity structure in geothermally active south-central Utah. *Journal of Geophysical Research: Solid Earth*, *127*(7), 1–23. https://doi.org/10.1029/2022jb024070

Wood, C. A., & Kienle, J. (1990). Volcanoes of north America: United States and Canada. In *Volcanoes of North America: United States and Canada* (1st edn.). Cambridge University Press. https://doi.org/10.1016/0031-9201(92)90173-s

Yang, X., & Gao, H. (2020). Segmentation of the Aleutian-Alaska subduction zone revealed by full-wave ambient noise tomography: Implications for the along-strike variation of volcanism. *Journal of Geophysical Research: Solid Earth*, *125*(11), e2020JB019677. https://doi.org/10.1029/2020JB019677

Yang, Y., & Ritzwoller, M. H. (2008). Characteristics of ambient seismic noise as a source for surface wave tomography. *Geochemistry, Geophysics, Geosystems*, *9*(2), Q02008. https://doi.org/10.1029/2007GC001814

Yao, H., Campman, X., de Hoop, M. V., & van der Hilst, R. D. (2009). Estimation of surface wave Green's functions from correlation of direct waves, coda waves, and ambient noise in SE Tibet. In *Physics of the Earth and planetary interiors, Issues 1–2* (Vol. 177, pp. 1–11). Elsevier BV. https://doi.org/10.1016/j.pepi.2009.07.002